Real time mass flow rate measurement using multiple fan beam optical tomography

R. Abdul Rahim[a],[*], L.C. Leong[a], K.S. Chan[a], M.H. Rahiman[b], J.F. Pang[a]

[a] *Process Tomography Research Group (PROTOM), Department of Control and Instrumentation Engineering, Faculty of Electrical Engineering,
Universiti Teknologi Malaysia, 81310 UTM Skudai, Johor, Malaysia*
[b] *Department of Mechatronics, Universiti Malaysia Perlis, Malaysia*

Abstract

This paper presents the implementing multiple fan beam projection technique using optical fibre sensors for a tomography system. From the dynamic experiment of solid/gas flow using plastic beads in a gravity flow rig, the designed optical fibre sensors are reliable in measuring the mass flow rate below 40% of flow. Another important matter that has been discussed is the image processing rate or IPR. Generally, the applied image reconstruction algorithms, the construction of the sensor and also the designed software are considered to be reliable and suitable to perform real-time image reconstruction and mass flow rate measurements.
© 2007, ISA. Published by Elsevier Ltd. All rights reserved.

1. Introduction

Process tomography is a developing measurement technology. Over the last decade, the concept of tomographic imaging was not restricted to the medical field; it has been successfully developed into a reliable tool for imaging numerous industrial applications. Sensors in the measurement system prove to be the most important part in acquiring the physical signal. The physical signal is then being converted, amplified and fed into the computer to obtain the internal behaviours of the investigated vessel. A conveyor with fast moving flow and rapid changing flow regime requires a sensor with very fast response and also a fast data acquisition rate in order to prevent data losses. The optical sensors have proved to possess the advantages of fast responce, high performance, low cost and low maintenance compared to electrical capacitance tomography.

2. Optical fibre for tomography imaging

Mass production of optical fibre has reduced the cost of the fibres significantly and more importantly the revolution brought simultaneous improvements and cost reduction in optoelectronic components. In the area of tomographic imaging, an initial investigation into using optic fibres as measurement sensors in pneumatic conveying was started in Sheffield Hallam University [8].

In using optical fibre for tomography imaging, the basic optical transmitter converts electrical input signals into modulated light for transmission over an optical fibre. Also, the light beam from the transmitter is being received by the receiver via the fibre optic. This configuration is being illustrated in Fig. 1. With regard to its small physical size, it is believed that using fibre optic will allow a higher number of optical sensors to be installed, thus achieving high-resolution measurement in optical tomography. It is also said that the optical fibre sensors provide wide bandwidth which enables measurements to be performed on high speed flowing particles [9].

3. Switch-mode fan beam method

Parallel projection and fan beam projection are two different types of sensor arrangement methods. For sensor arrangement method using parallel projection method, each transmitter and receiver only corresponds to each other. While for the fan beam projection method, there may be more than one receiver corresponding to a single or multiple light sources [1].

---

* Corresponding address: Universiti Teknologi Malaysia, Research Management Centre, 81310 UTM Skudai, Johor, Malaysia. Tel.: +60 7 5537804; fax: +60 7 5566177.

E-mail addresses: ruzairiabdulrahim@yahoo.co.uk, Ruzairi@fke.utm.my (R. Abdul Rahim).
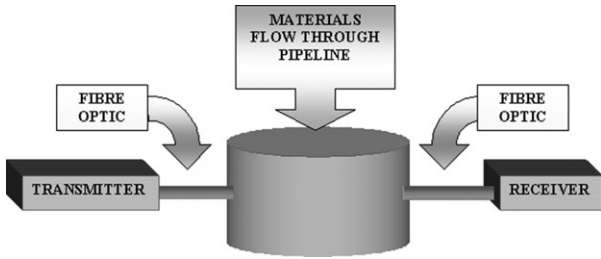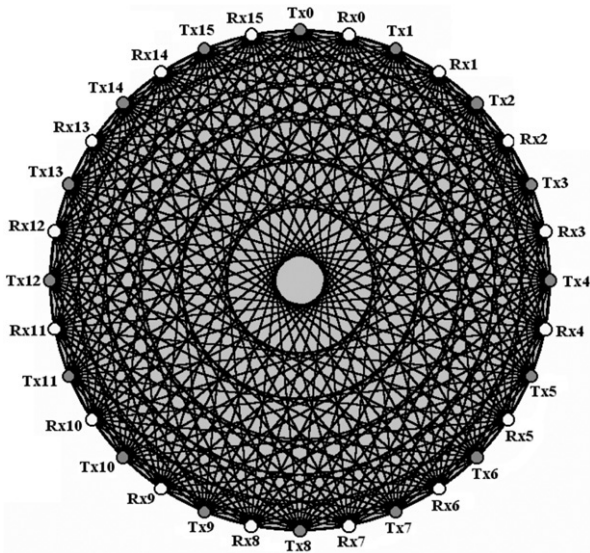
Fig. 1. Fibre optic configuration.

Fig. 2. Sensor configuration in switch-mode fan beam projection method.

In the switch-mode fan beam method, a multiplexing source is used and all the receivers produce the signals corresponding to each multiplexed source. Fig. 2 shows the sensors' configuration of fan beam projection method whereby the transmitters and receivers are arranged alternately.

By assuming that the transmitter is the LED which has a wide transmission angle of 140°, the LED or Tx_n will be turned on subsequently whereby the subscript n here represents different LEDs [3].
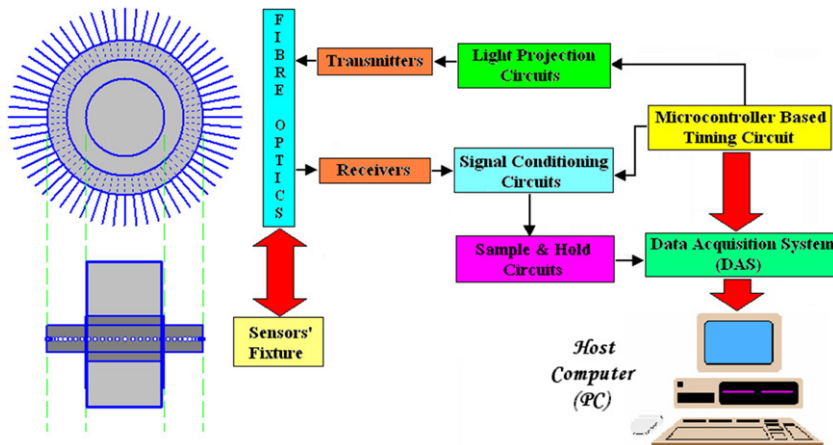
4. Hardware construction

A typical optical tomography system consists of the sensors' array, signal control and conditioning circuit and also the display unit, namely the computer. In this research, instead of mounting the transmitters and receivers straight to the pipeline as being done by Chan [2], Abdul Rahim [1], the optical fibres are applied. A total of 64 fibre optics are used, with 32 connected from the sensor's fixture (at the circumference of the flow rig) to the emitters and the other 32 fibre optics are connected to the receivers. The topology of the hardware construction is shown in Fig. 3.

By referring to Fig. 3, the microcontroller is used to control the duration of light projection, sample and hold digital input and data acquisition system (DAS) synchronization signals. Through the fibre optics, photodiodes detect the physical signals (light beams) from the transmitters. In the signal conditioning circuit, the physical signals are being converted into voltage readings and then amplified. The analogue signals go through the sample and hold circuit before being transferred into DAS. DAS then converts the analogue signals into digital signals. These digital signals are sent to the PC for image reconstruction.

4.1. Multi-projection technique

A new technique of implementing the switch-mode fan beam method is being investigated in this paper. The technique mentioned is the 2-projection technique. Preliminary experiments show that the maximum achievable emission angle for the fibre optic transmitter is about 30°, after the fibre optic is being lensed. 32 fibre optic transmitters are used in this research; thus in order to make sure that the emission angle is approximately the same, each of the fibre optic emission angles is tested experimentally. The experimental method is illustrated in Fig. 4.

The fibre optic for the transmitter will be lensed until both the Rx receive signals. This means that the emission angle has reached 30°. All the 32 fibre optics for transmitters' angles will be determined experimentally this way.

Fig. 3. Topology of the hardware construction.

Table 1
Configuration of transmitters and corresponding receivers

| Transmitter	Receiver						Transmitter	Receiver					
Tx0	Rx13	Rx14	Rx15	Rx16	Rx17	Rx18	Tx16	Rx29	Rx30	Rx31	Rx0	Rx1	Rx2
Tx1	Rx14	Rx15	Rx16	Rx17	Rx18	Rx19	Tx17	Rx30	Rx31	Rx0	Rx1	Rx2	Rx3
Tx2	Rx15	Rx16	Rx17	Rx18	Rx19	Rx20	Tx18	Rx31	Rx0	Rx1	Rx2	Rx3	Rx4
Tx3	Rx16	Rx17	Rx18	Rx19	Rx20	Rx21	Tx19	Rx0	Rx1	Rx2	Rx3	Rx4	Rx5
Tx4	Rx17	Rx18	Rx19	Rx20	Rx21	Rx22	Tx20	Rx1	Rx2	Rx3	Rx4	Rx5	Rx6
Tx5	Rx18	Rx19	Rx20	Rx21	Rx22	Rx23	Tx21	Rx2	Rx3	Rx4	Rx5	Rx6	Rx7
Tx6	Rx19	Rx20	Rx21	Rx22	Rx23	Rx24	Tx22	Rx3	Rx4	Rx5	Rx6	Rx7	Rx8
Tx7	Rx20	Rx21	Rx22	Rx23	Rx24	Rx25	Tx23	Rx4	Rx5	Rx6	Rx7	Rx8	Rx9
Tx8	Rx21	Rx22	Rx23	Rx24	Rx25	Rx26	Tx24	Rx5	Rx6	Rx7	Rx8	Rx9	Rx10
Tx9	Rx22	Rx23	Rx24	Rx25	Rx26	Rx27	Tx25	Rx6	Rx7	Rx8	Rx9	Rx10	Rx11
Tx10	Rx23	Rx24	Rx25	Rx26	Rx27	Rx28	Tx26	Rx7	Rx8	Rx9	Rx10	Rx11	Rx12
Tx11	Rx24	Rx25	Rx26	Rx27	Rx28	Rx29	Tx27	Rx8	Rx9	Rx10	Rx11	Rx12	Rx13
Tx12	Rx25	Rx26	Rx27	Rx28	Rx29	Rx30	Tx28	Rx9	Rx10	Rx11	Rx12	Rx13	Rx14
Tx13	Rx26	Rx27	Rx28	Rx29	Rx30	Rx31	Tx29	Rx10	Rx11	Rx12	Rx13	Rx14	Rx15
Tx14	Rx27	Rx28	Rx29	Rx30	Rx31	Rx0	Tx30	Rx11	Rx12	Rx13	Rx14	Rx15	Rx16
Tx15	Rx28	Rx29	Rx30	Rx31	Rx0	Rx1	Tx31	Rx12	Rx13	Rx14	Rx15	Rx16	Rx17
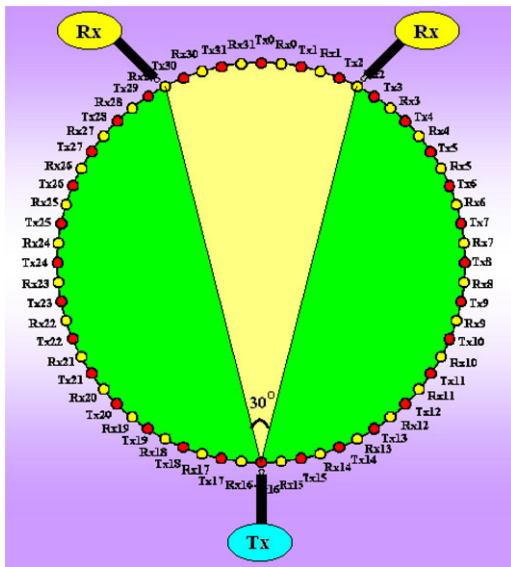
Fig. 4. Determining emission angle.

Due to the limitation of the fibre optic's emitting angle, it is indeed an advantage to implement multiprojection to the light projecting system without worrying about the overlapping of received photodiode signals. For the 32 transmitter model, Tx_n and Tx_{16+n} will project light at the same time, for example, Tx_0 and Tx_{16}, Tx_1 and Tx_{17} etc. will project light at the same time. 16 sets of projection will complete one frame of light emission. This will also minimize the total time for one frame of data to be sent to the computer thus obtaining a higher data acquisition rate.

4.2. Multiple fan beam projection geometry

Implementation of the multiple projection technique using switch-mode fan beam method yields two projection geometries which are the 2-projection geometry and the 4-projection geometry. When two or four transmitters project light at the same time, the total time to complete one frame of data acquisition will be shorter, thus it is believed that both
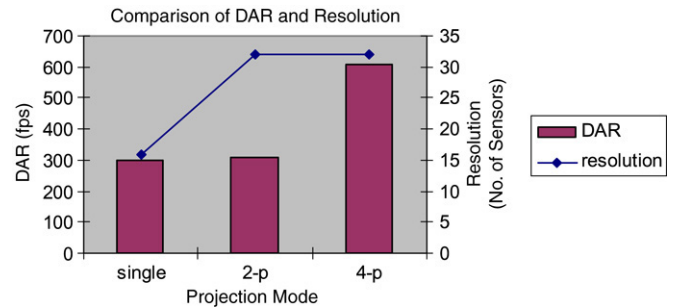

Fig. 5. Comparison of DAR and resolution.

these techniques are able to achieve better timing performances in data acquisition process compared with the conventional single light projection.

The above multiple fan beam projection achievement can be further verified by comparing the number of sensors and DAR obtained by Chan [2] with the results achieved in this research, whereby the multiple projection technique has a capability to increase the resolution of the hardware system (a higher number of sensors installed) and at the same time increasing the DAR (shorter time needed for data conversion in one frame). The graph shown in Fig. 5 represents the improvement for the DAR achieved by multiple projection technique in this research when compared to the single projection result achieved by Chan [2].

The projection geometry of both the techniques is shown in Fig. 6.

Considering that the 32 transmitters and 32 receivers are arranged alternately in clockwise starting from Tx0, Rx0, Tx1, Rx1 until Tx31 and Rx31, the transmitters emit light according to this arrangement sequence. At a transmission angle of 30°, each projection provides six light beams (six views) which will be received by the corresponding receivers as tabulated in Table 1.

For the 2-projection technique, sixteen sets of projections will complete one frame of light emission whereby Tx_n and Tx_{16+n} (with n as the respective number projection ranging from 0 to 15) will transmit light at the same time. As for the 4-projection technique, eight sets of projections will complete
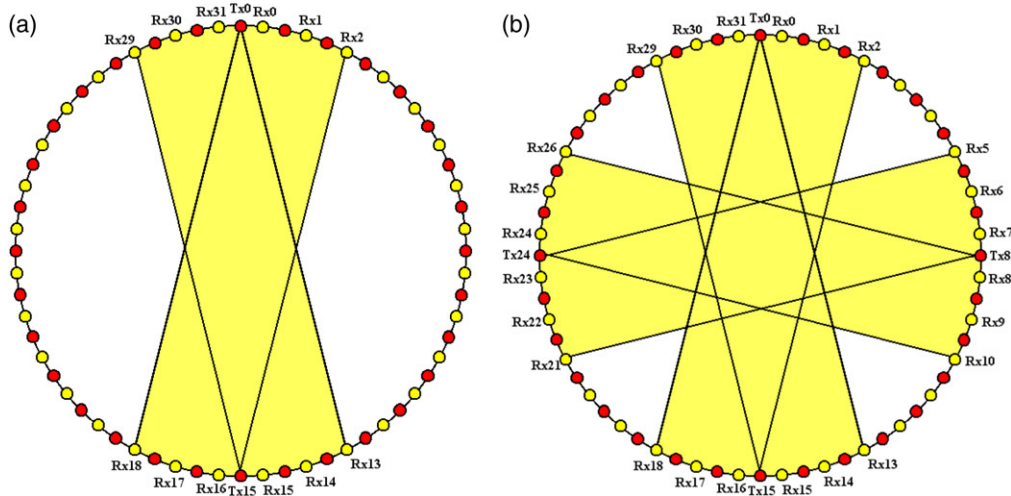
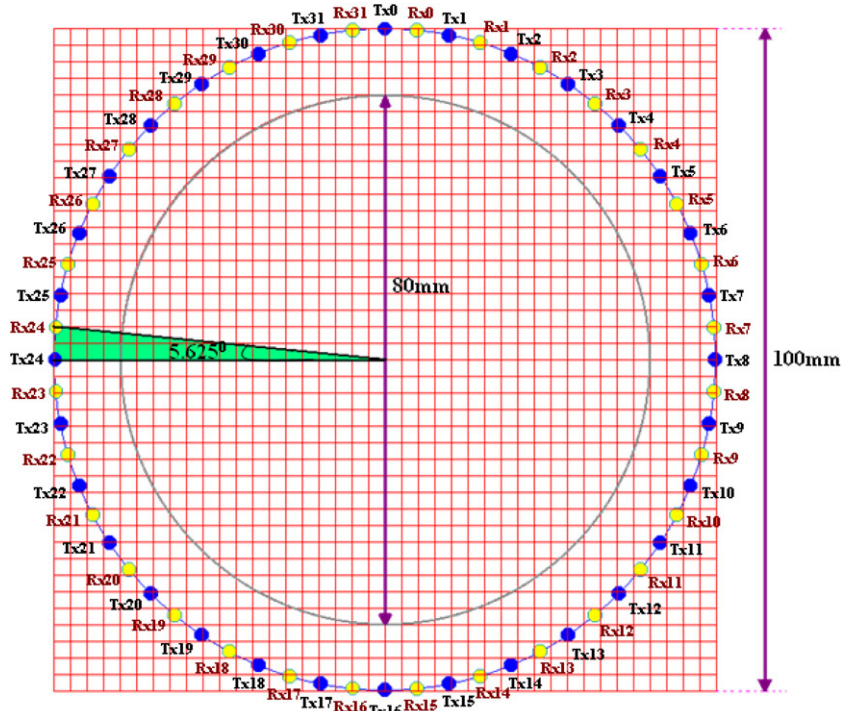Fig. 6. Multiple projection geometry. (a) 2-projection (b) 4-projection.

Fig. 7. Optical fibre sensors arrangement on sensor's fixture.

one frame of light emission with Tx_n, Tx_{8+n}, Tx_{16+n} and Tx_{24+n} (taking n as the respective number projection ranging from 0 to 7) transmitting light at the same time.

The projection geometry of the sensors determines the relationship between the sensors' arrangements and its mathematical modeling. In this research, thirty-two pairs of optical sensors are employed. The optical sensors are divided into thirty-two infrared transmitters and thirty-two photodiode receivers which are placed alternately. These optical sensors are each coupled to separate fibre optics to the periphery of the sensor's fixture. The diameter of the sensor's fixture which mounts the fibre optics is 100 mm and its circumference equal to 314.2 mm.

By distributing the fibre optics evenly around the circumference of the fixture as shown in Fig. 6, the angle between each emitter and its adjacent receiver viewed from the centre of the circle is 5.625° (dimensions not to scale in figure).

The optical fibre sensors arrangement in Fig. 7 is seen from the top view. The sensor's fixture is designed to be bigger than the pipeline used. Tx and Rx represent the respective transmitters and receivers as they are arranged alternately in clockwise direction, starting from Tx0 and ending at Rx31. The 80 mm dimension is the diameter of the investigated pipe and the red gridlines are the 32×32 mapping resolution which is applied in solving the forward and inverse problems.
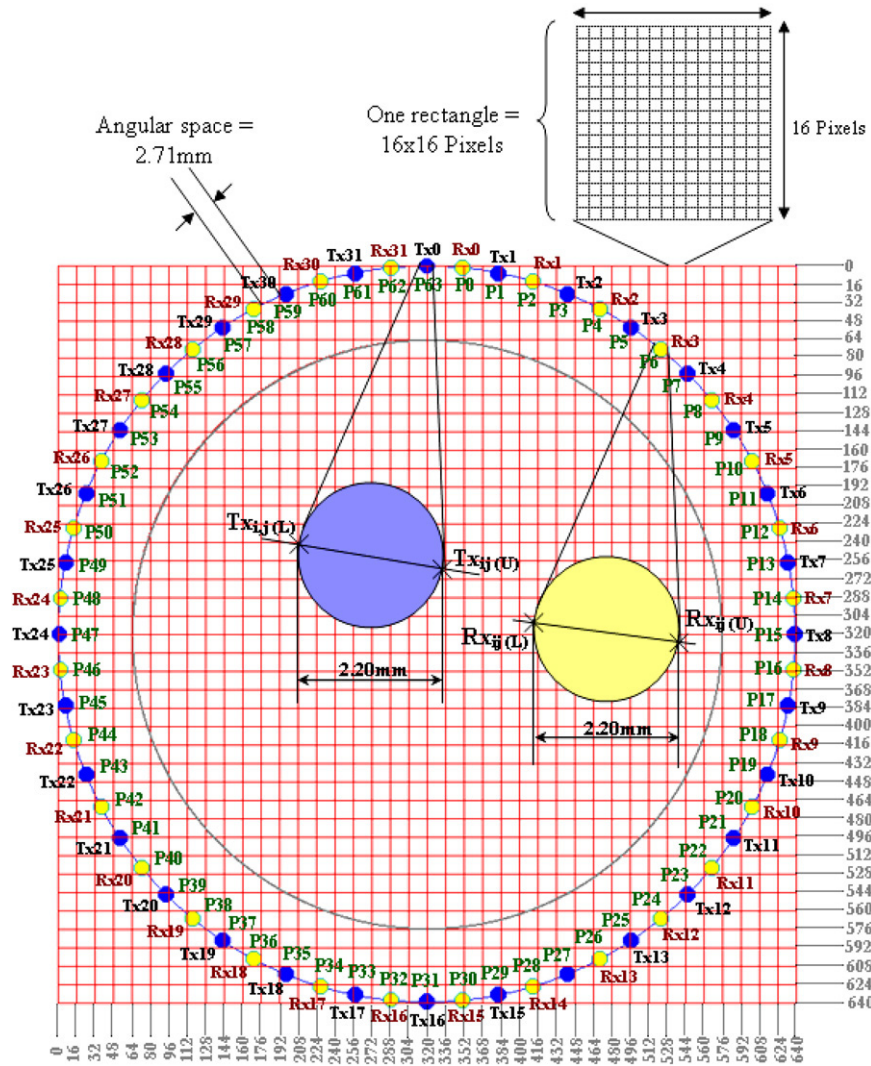
Fig. 8. Optical fibre sensors mapping platform.

To simplify the mapping of optical fibre sensors to the two-dimension image plane, it is assumed that diameters of both optical fibre sensors (transmitters and receivers) are the same which is 2.20 mm. This assumption is made because the size of the fibre optic's inner core is 1 mm and after they are lensed, the surface of the inner core has an approximate diameter of 2.20 mm. A two-dimension image plane which is made up of 640×640 pixels in Fig. 8 serves as the mapping platform for the optical fibre sensors.

The mapping of sensors on the image plane is important in solving the forward problem. Through Visual C++ programming, the image plane is set to 640×640 pixels using two-dimensional Cartesian coordinates. The top-left corner coordinate is at (0, 0) and the right-bottom end coordinate is (640, 640) as shown in Fig. 8. To map the sensors, labeled as P0–P64, calculations are done by dividing the circle into four quadrants as presented in Fig. 8.

For all the quadrants in Fig. 9, sensors P0–P16 can be mapped by using the drawings and equations in Table 2, whereby:

$P_n.x =$ the xth coordinate of the nth sensor.
$P_n.y =$ the xth coordinate of the nth sensor.
$r =$ the radius of the circle which is 320 pixels.
$\theta =$ angle between emitter and its adjacent receiver viewed from the centre of the circle, which is 5.625°.
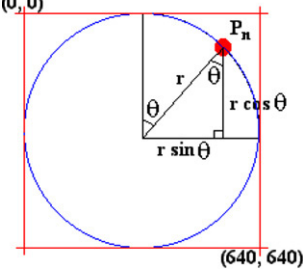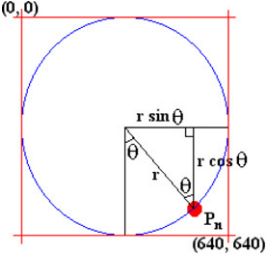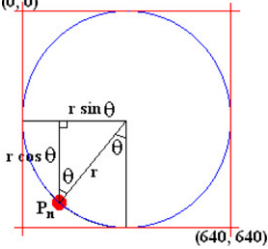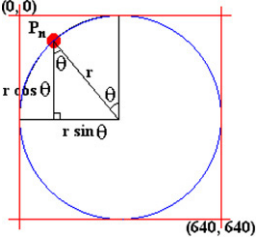
By using the mapping methods as above, the computer generated coordinates of all the sensors are tabulated in Table 3.

From the 640×640 pixels, the resolution of the plane is divided into 40×40 rectangles. Each rectangle has a total of 256 pixels. By definition, pixel represents the smallest unit of an image and resolution refers to the clarity or sharpness of an image, initiated by the number of pixels per square inch on a computer-generated display. When the transmitters and receivers are distributed evenly on the periphery of the sensor's fixture, the equispaced interval [5] between each transmitter and the subsequent receiver is 2.71 mm by using Eq. (1).

$$E.S = \frac{C - (2.20)n}{n} \tag{1}$$

whereby:

Table 2

Mapping sensors to image plane by using Cartesian coordinates

Quadrant	Mathematical drawing	Equations
Q1		$P_n.x = r + r\sin\theta$ $P_n.y = r - r\cos\theta$
Q2		$P_n.x = r + r\sin\theta$ $P_n.y = r + r\cos\theta$
Q3		$P_n.x = r - r\sin\theta$ $P_n.y = r + r\cos\theta$
Q4		$P_n.x = r - r\sin\theta$ $P_n.y = r - r\cos\theta$

$E.S$ = Equispaced interval (mm).
C = Circumference (mm).
n = A total of 64 optical fibre sensors.

These predetermined geometrical coordinates and rectangles will be useful in sensor modelling and generating sensitivity maps.

4.3. Sensitivity maps

From the fan beam projection properties [1], it is known that the fan beam projection can be seen as a point source of radiation that emanates as a fan shaped beam. The emanation covers in many directions in different angles. For a given source and detector combination, functions are calculated that describe the sensitivity of each source and measurement pair to changes in optical properties within each pixel of the model [10]. Thus, when the projection beam is mapped onto the two-dimensional
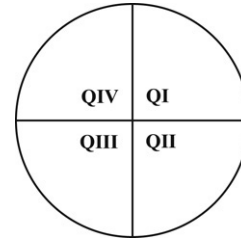

Fig. 9. Dividing the circle into four quadrants.

image plane, each light beam will spread across each rectangle in different weights as illustrated in Fig. 10.

The solution of forward problem generates a series of sensitivity maps. And the inversion of these sensitivity matrixes therefore provides a reconstruction of the optical properties [10]. Basically, the number of generated sensitivity maps is dependent to the number of projections for the sensors. No matter whether the applied projection method is the 2-projection or 4-projection method, each light beam must be sampled individually. Therefore, for the thirty-two transmitters and the corresponding six receivers which receive light per emission of each transmitter, the total projections are 192. This means that there will be 192 sensitivity maps generated as well. Before these sensitivity maps can be used for image reconstruction, they must be normalized first.

Normalization of sensitivity maps is done when there is no simple linear relationship between the weight distributions in a rectangle for different light projections. For example, the rectangle (25, 30) might have certain percentage of light passing through for the light beam of transmitter 10 and receiver 25. When transmitter 0 emits light to receiver 16, this light beam might pass through rectangle (25, 30) with a different weight distribution. If there are other light beams passing through the same pixel as well, the weight distribution of the pixel will become complicated. Thus, it is necessary to build a general relationship between the pixels and all the projection beams that pass through the pixels. A simple approach to normalize the rectangle values in this research is engaged in a similar manner as normalizing the pixel values in ECT so that they have the values of zero and one when the rectangle contains the lower and higher weight distributions respectively.

As a reference to map the sensitivity maps onto the 2-dimension image plane, Fig. 8 is being referred. From the 640 × 640 pixels plane, there are gridlines to divide the pixels into 40 × 40 rectangles where each rectangle contains 16 × 16 pixels. When a light projection maps on the rectangles, a certain number of pixels in once particular rectangle will be dubbed into either '1' for pixels covered with light beam or '0' for pixels not covered by light beam. The total number of '1' pixels of light beam will be counted for each rectangle which will be then represented as the total weight of the rectangle involved.

In image reconstruction, the actual area of flow is from pixel 64 to pixel 575 in x-axis and y-axis. In this section the image plane is reconfigured so that all calculations and scanning of pixels are done only for the part of the actual flow area. This is being done to avoid wasting unnecessary time and resources used to calculate and scan the whole 640 × 640 pixels. The

Table 3
The full coordinates of all the sensors from P0–P63

| Sensor	Coordinate	Sensor	Coordinate	Sensor	Coordinate	Sensor	Coordinate
P0	(351, 2)	P16	(638, 351)	P32	(289, 638)	P48	(2, 289)
P1	(382, 7)	P17	(633, 382)	P33	(258, 633)	P49	(7, 258)
P2	(412, 14)	P18	(626, 412)	P34	(228, 626)	P50	(14, 228)
P3	(442, 25)	P19	(615, 442)	P35	(198, 615)	P51	(25, 198)
P4	(470, 38)	P20	(602, 470)	P36	(170, 602)	P52	(38, 170)
P5	(497, 54)	P21	(586, 497)	P37	(143, 586)	P53	(54, 143)
P6	(523, 73)	P22	(567, 523)	P38	(117, 567)	P54	(73, 117)
P7	(546, 94)	P23	(546, 546)	P39	(94, 546)	P55	(94, 94)
P8	(567, 117)	P24	(523, 567)	P40	(73, 523)	P56	(117, 73)
P9	(586, 143)	P25	(497, 586)	P41	(54, 497)	P57	(143, 54)
P10	(602, 170)	P26	(470, 602)	P42	(38, 470)	P58	(170, 38)
P11	(615, 198)	P27	(442, 615)	P43	(25, 442)	P59	(198, 25)
P12	(626, 228)	P28	(412, 626)	P44	(14, 412)	P60	(228, 14)
P13	(633, 258)	P29	(382, 633)	P45	(7, 382)	P61	(258, 7)
P14	(638, 289)	P30	(351, 638)	P46	(2, 351)	P62	(289, 2)
P15	(639, 320)	P31	(320, 639)	P47	(1, 320)	P63	(320, 1)
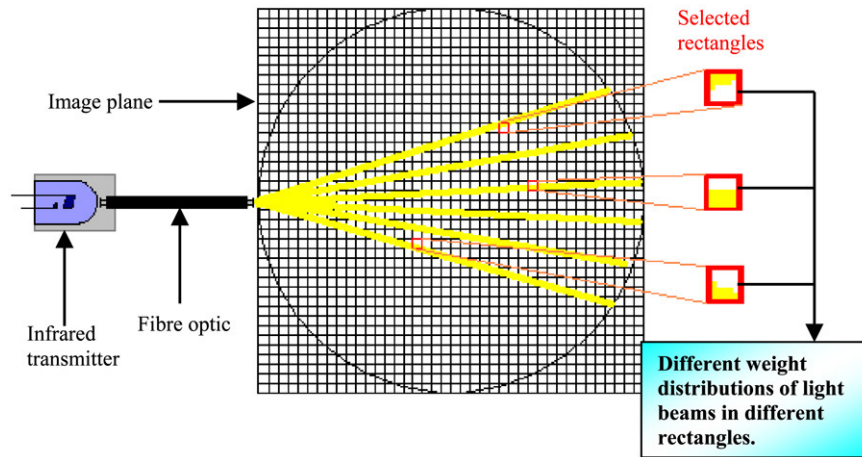
Fig. 10. Fan beam projection map.

resolution of the actual image plane thus becomes 32×32 in image reconstruction which contains 512×512 pixels. This explanation can be further explained graphically in Fig. 11.

After the actual flow area is being identified, the sensitivity maps are generated using Visual C++ programming language as shown in Eq. (2).

$$S_{i,j}(x, y) = \sum_{a=0}^{511} \sum_{b=0}^{511} P_{x,y}(a, b)$$

$$\begin{cases} P_{x,y}(a, b) = 1; & \text{if black} = \text{changed} \\ P_{x,y}(a, b) = 0; & \text{if white} = \text{unchanged} \end{cases} \quad (2)$$

whereby:

$S_{i,j}(x, y) =$ sensitivity map of light beams for all transmitters and receivers.
$P_{x,y}(a, b) =$ an array to represent the total black pixels in rectangle-xy.
a and $b =$ the ath column and bth row of the pixels in the actual flow plane.
x and $y =$ the xth column and yth row of the 32×32 rectangles or resolution.

Next is to sum and normalize all the 192 sensitivity maps using the following two approaches:

1. Summing the maps according to the weights of the same rectangles from all projections and normalizing the maps (rectangle-based normalization).
2. Summing the maps based on weights of all the rectangles for individual light projection and normalizing the maps (projection-based normalization).

The rectangle-based normalization is to total up all the total black pixels from all different projections in a same rectangle using Eq. (3) and normalize the maps according to Eq. (4).

$$T1(x, y) = \sum_{i=0}^{32} \sum_{j=0}^{16} S_{i,j}(x, y) \quad \begin{cases} 0 \leq x < 32 \\ 0 \leq y < 32 \end{cases} \quad (3)$$

$$N1_{i,j}(x, y) = \begin{cases} \dfrac{S_{i,j}(x, y)}{T1(x, y)}; & \text{for } T1(x, y) > 0 \\ 0; & \text{for } T1(x, y) = 0 \end{cases} \quad (4)$$
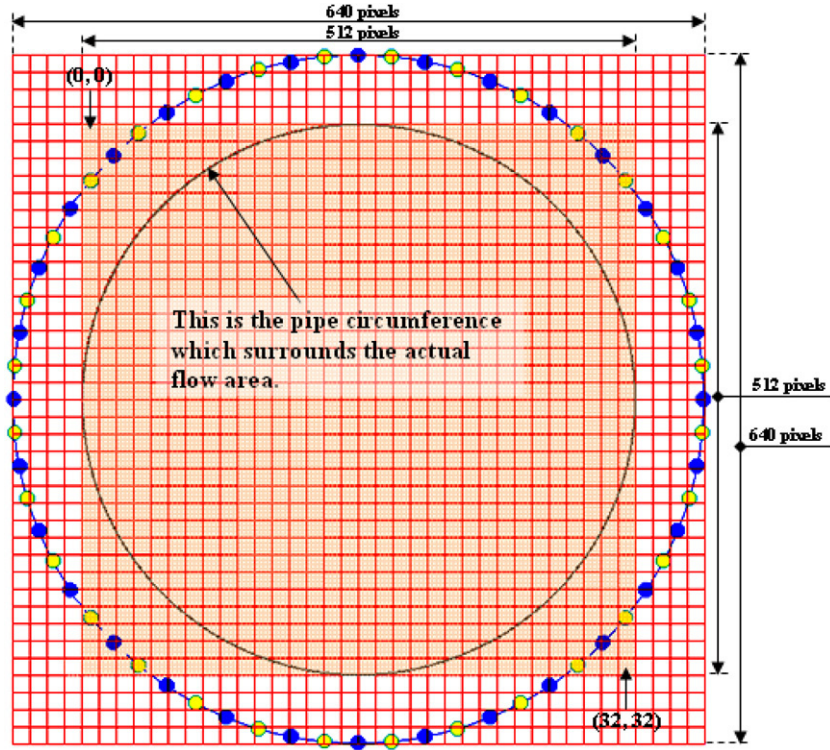
whereby:

Fig. 11. The actual flow image plane.

$T1(x, y) =$ the total or sum of the same element in rectangle-xy obtained from the 192 sensitivity maps.

$S_{i,j}(x, y) =$ the 192 sensitivity maps.

$N1_{i,j}(x, y) =$ the normalized sensitivity maps for light beams of all Tx ($0 \le i < 32$) to Rx ($0 \le j < 6$) using the rectangle-based normalization.

Meanwhile, by using the projection-based normalization, the total weights of pixels for all rectangles (32 rectangles) for each light projection is being summed by using Eq. (5) and then normalized as stated in Eq. (6).

$$T2(i, j) = \sum_{x=0}^{32} \sum_{y=0}^{32} S_{i,j}(x, y) \tag{5}$$

$$N2_{i,j}(x, y) = \frac{S_{i,j}(x, y)}{T2(i, j)} \quad \begin{cases} T2(i, j) > 0 \\ 0 \le i < 32 \\ 0 \le j < 6 \end{cases} \tag{6}$$

whereby:

$T2(i, j) =$ the total of pixel weights for all rectangles in individual light projection.

$S_{i,j}(x, y) =$ the 192 sensitivity maps.

$N2_{i,j}(x, y) =$ the normalized sensitivity maps for light beams of all Tx to Rx using the projection-based normalization.

Since the normalized maps generated in Eqs. (4) and (6) has a total of 192 maps each.

5. Results and discussions

5.1. Mass flow rate results

Mass flow rate or MFR can be defined as the number of grams or kilograms of flow that flows pass a given cross-sectional area per second (unit of g/s or kg/s). For a tomographic system with two layers of sensors (upstream and downstream), the mass flow rate of the flow can be obtained by multiplying the density of the flow material (g/m^3) with velocity of the flow (m/s) and also with the cross-sectional of the pipe which the flowing objects flow through (m^2). Here, the velocity of the flow is being determined by performing cross-correlation of the concentration profiles for the upstream and downstream sensors. However, for the single layer of sensors implemented using the optical fibre fan beam method in this research, the velocity of the flowing object cannot be determined by using the cross-correlation method.

Instead, an alternative approach introduced by Ruzairi [8] is taken to obtain the mass flow rate for the solid/gas flow. First, the solid material for the flow system must be determined because different solid materials have different densities and sizes and therefore yields different flow properties. Second, by using the selected solid material, the specified flow rig must be calibrated. This will result in a relation between the concentration measurements and the manually obtained mass flow rates. The manually obtained mass flow rates are the actual mass flow rates for the flowing system.

Instead of using the gravity conveying system with rotary screw feeder, a range of filters are designed and used. This is to solve the problems highlighted by Chan and Ruzairi [3]
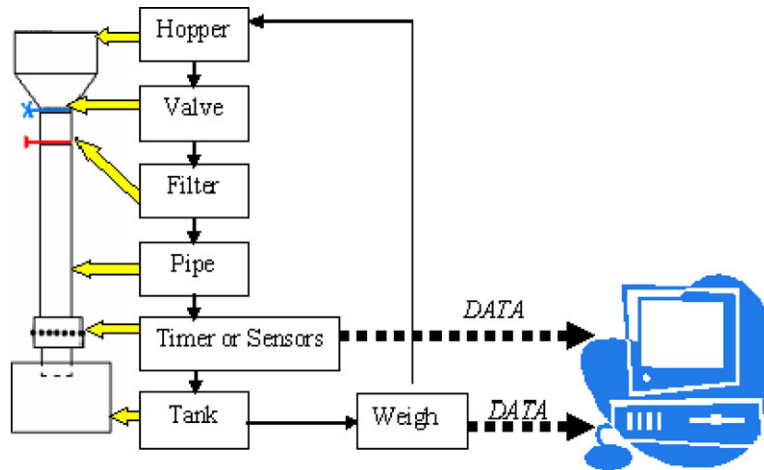
Fig. 12. Flow rig calibration process.

whereby the resulting flow of the rotary screw feeder can cause un-uniformed flow. The main aim to investigate the MFR in this research is to provide an estimate of the range of mass flow that will allow the optical fibre sensors to perform reliably. The flow diagram of the calibration process is shown in Fig. 12 while the experimental properties of the dynamic flow system are being identified as follows:

5.2. Experimental conditions

Flow rig: Gravity flow rig in experimental scale.
Diameter of pipe used: 80 mm.
Length of pipe until the sensors: 1.2 m.
Flowing material: Plastic beads.
Mean particle size of the plastic beads: Nominal diameter of 3 mm.
Filters: 10%, 20%, 30%, 40%, 50%, 60%, 70%, 80%, 90% of the flow regime.
Sensor array structure: 32 optical fibre transmitters and 32 optical fibre receivers.
Photo-sensors: Infrared emitters and photodiode receivers.
Peak wavelength of light source: 880 nm.
Type of projection: 4-projection switch-mode fan beam projection technique.
Pixel grids/resolution: 32×32.

With reference to the Fig. 12, the flow lines represents the flow of the calibration process while the dotted lines show the flow data to the computer to be analysed. First, the plastic beads are manually filled into the hopper. At this time, the valve is still closed to prevent flow from falling through the pipeline. Next, the filter is inserted and then the timer is reset. When the valve is opened, the plastic beads will flow through the pipeline into the tank and the timer will start to count when it senses the first particle that intercepts its light beam.

The timer used here comprised the infrared projection circuits, photodiode receiver amplifying circuits, logic gates and comparator circuits. The output of the timer is connected to an oscilloscope to monitor the output waveform; the output will stay at 'high' until the light beams from the infrareds to the photodiodes are being intercepted. The output will stay at
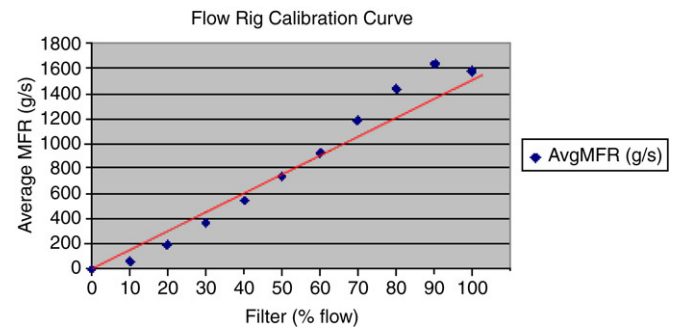

Fig. 13. Flow rig calibration curve for plastic beads.

'low' until the light beams are not intercepted or when the user stops the oscilloscope. Thus, the total time taken for the flow to commence is the duration of negative pulse width of the output waveform. The timer application can perform better than using the stopwatch because the start and stop time of the stopwatch is user-operated and there is bound to be inaccuracy due to human error and delays.

When the flow has stopped, the collected plastic beads in the tank is weighed using the weighing machine. The weight of the measured plastic beads and the total time needed for the flow are keyed into the computer for data analysis. After that, the whole process is repeated until all the filters have beeen used. Using a simple technique to obtain the best results in experiments, the process is repeated five times for each filter to get an average mass flow rate. The graph for average MFR versus the filters is illustrated in Fig. 13.

By referring to Fig. 13, although the points in the graph could be fitted by a higher order polynomial, a first order polynomial has been fitted to the data to simplify the equation for easier manipulation and calculation [8]. The equation of the linear regression line [4] is formed using Eq. (1).

$$\text{Average MFR (g/s)} = 23.256 * [\text{Filter (\%flow)}] . \tag{7}$$

The sampling time is set at 5 kHz to obtain 100 sets of concentration measurements. After the flow rig calibration has been completed, the timer is uninstalled and the optical fibre sensor array is attached to the pipeline (the same location as the
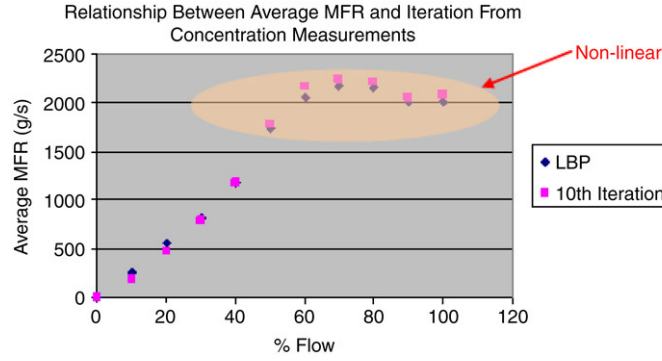
Fig. 14. Relationship between average MFR and iteration number.

Table 4
Percentage of flow obtained from concentration profiles

%Flow	MFR (g/s)	
	LBP	10th iteration
0	0	0
10	265.79	190.729
20	554.39	475.952
30	824.98	784.808
40	1171.3	1179.454
50	1743.7	1777.036
60	2060.6	2163.671
70	2176.7	2240.975
80	2161.6	2215.693
90	2008.8	2053.892
100	2016.3	2089.983

timer). The whole process in Fig. 11 is repeated, only now the sensors are used to capture the voltage loss to perform image reconstruction. Through the data acquisition system, 100 sets of data are taken per solid/gas filter. The sampling time is set at 5 kHz. These sensor losses are processed to obtain 100 sets of concentration measurements. The average concentration profile is obtained by adding all the concentration measurements and the bulk value of concentration profile is divided by the number of datasets, which are 100 in this case. There are 32×32 pixels used to form the reconstructed tomogram, thus in order to obtain the percentage of flow for the concentration profile Eq. (8) is implemented.

$$\%\text{Flow} = \left(\frac{\sum_{i=1}^{1024} \text{Vlbp}[i]}{5120} \right) * 100 \qquad (8)$$

whereby:

%Flow = percentage of flow obtained.
Vlbp[i] = the concentration profile of the image at ith pixel.

Eq. (6) to obtain the average MFR of the flow. Two image reconstruction algorithms are used to process the measured sensor values into concentration profiles [6]. Table 4 shows the results obtained from real-time data acquisition and Fig. 14 illustrates the relationship of the average MFR obtained for the LBP and iterative reconstruction algorithm.
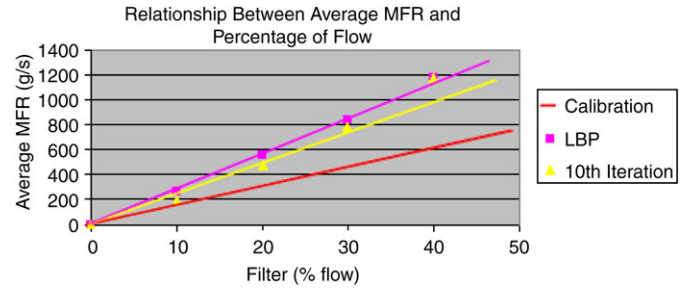

Fig. 15. Relationships between average MFR and percentage of flow.

Table 5
Slopes and corrective coefficients for MFR graphs

Graph property	Calibration	LBP	10th iteration
Slope, m	23.256	26	24.211
Slope ratio, r	–	0.894	0.961
Linear equation	$y = 23.256x$	$y = 26x$	$y = 24.211x$
Corrective coefficient, K	–	0.894	0.961

It is observed that the average MFR acquired by the sensors is only linear up to the range of 40% flow. This verifies the results obtained from the static flow model experiment using half flow whereby the half flow or 50% of flow cannot be measured by the sensors [6]. For further analysis, the linear range of the average MFR from flow rig calibration, LBP algorithm and the 10th iteration are integrated in Fig. 15.

It is observed that the linear regression of the calibration, LBP and the 10th iteration lines have different slopes each. The closer the graph is to the calibration line, the more accurate the MFR is. A corrective coefficient is needed for the LBP and 10th iteration graphs so that they behave the same way as the calibrated data. To find the stated corrective coefficient, the slopes of all the three graphs have to be calculated. The slopes and coefficients needed for the graphs are listed in Table 5 whereby slope ratio for calibration is not available because this slope will be used as reference for comparison with LBP and 10th iteration slopes.

The y and x term in the linear equations represents the y-axis and x-axis of the MFR graphs. From the table, the slope ratio, r of the 10th iteration is smaller than the r of LBP, thus it can be concluded the 10th iteration image reconstruction provides a more accurate image than the LBP with reference to

Table 6
Investigation of image processing rate using different computer speeds

Computer properties	ISA slot availability	Image processing rate (fps)			
		LBP	1st iteration	5th iteration	10th iteration
Intel Pentium III, 667 MHz	Yes	12	8	3	2
Intel Pentium III, 933 MHz	Yes	24	15	6	4
Intel Pentium IV, 1.5 GHz	No	77	35	11	6
Intel Pentium IV, 2.4 GHz	No	136	63	20	11

the calibration graph. By applying the calculated K values into both image reconstruction algorithms, the new linear equation for the graphs is presented in Eq. (9).

$$y_{LBP} = (26.000 * x_{LBP}) * 0.897 \tag{9a}$$

$$y_{10th\ Ie} = (24.211 * x_{10th\ Ie}) * 0.961. \tag{9b}$$

Overall, the conclusion that can be drawn is that for the plastic bead flow using the gravity flow rig on an experimental scale, the optical fibre sensors implemented in this research are suitable to measure mass flow rates at the range of zero to not more than 40% of the flow. The slope ratio, r, obtained proved that the iterative method results in a better image for low density flows.

5.3. Image processing rate (IPR)

The image processing rate is the comparative measurements of the time taken to process and display the image using different reconstruction algorithms. Based on the optimization concept, a programmer should use fewer codes to accomplish the application and spend the minimum time to execute the program written. In terms of optimizing the execution of image reconstruction and displaying the image in bitmaps, a suitable timer and image display method are essential. In this research, the Device Dependent Bitmap (DDB) method is used to draw the tomogram because it is considered the fastest way to construct and display an image compared to the other methods [7]. DDB is controlled by the device driver of display card and can only be displayed on the device with the correct configuration. By comparing to the Device Independent Bitmap (DIB), DDB can save processing time because DIB has to be converted to DDB before displaying the image onto screen.

Next, is the concern of using the suitable timer to execute the counting of time needed to process and display the image. From the research done by Pang [7], regarding the timing functions found in Win32 library he has found out that the *high performance timer* is the only timer that has the ability to measure a minimum time resolution of 1 μs while the rest of the timers such as the *GetTickCount, Clock, timeGetTIme* and *_ftime* timers can only count the minimum time resolution of 1 ms. Pang [7] has also done an experiment to find the standard deviation of the timers by counting a routine's execution time using 20 sets of data. The results showed that the high performance timer has the lowest standard deviation value which means that this timer is good in repeatability and has the highest precision. Thus, based on his deduction, the high performance timer is being applied in this research.

Although the functions above are being selected to execute the image processing and display in a most optimized manner, it is found out that the speed of the image processing rate is dependent on the processing speed of the computer used. The image processing rate for the image reconstruction using LBP and iterative algorithms is investigated using different speed specifications of the computer. The result of the investigation is tabulated in Table 6.

During the investigation of the image processing rate, the same GUI program is being run in four different computers with different processor speed. It is noticed that the IPR increases with the increase of processor's speed as shown in Table 6. From the table also, the ISA slot availability is being checked for each of the computer because the available Keithley DAS1802HC data acquisition card in the laboratory requires the ISA slot for communication. Recent Intel Pentium IV computers have only the PCI slots and therefore are not suitable to be used for a real-time data acquisition process although they have the potential to achieve a higher image processing rate. Instead, the Intel Pentium III 933 MHz computer is used because it has the fastest processor speed among the computers with ISA slots. As a conclusion, it is thus proved that using the same programming, different computer speeds will result in different image processing rates.

6. Conclusions

From the dynamic experiment of solid/gas flow using the plastic beads in a gravity flow rig, the designed optical fibre sensors are reliable in measuring the mass flow rate below 40% of flow.

Another important matter that has been discussed is the image processing rate or IPR. The IPR is dependent on the optimization of certain functions used in processing the image using different image reconstruction algorithms and also displaying the tomogram GUI. This research has opted for the most optimized applications of DDB display method and also the high performance timer which is able to measure the minimum time resolution of 1 μs. The only factor that limits the IPR of this research is that fastest available processor speed of the computer with ISA slot is the Intel Pentium III 933 MHz, which has a slow processor speed compared to the Intel Pentium IV processors. The choice of computer is limited because the Keithley DAS 1802HC requires communication with the ISA slot and only the Intel Pentium III processors have this feature. Generally, the applied image reconstruction algorithms, the construction of the sensor and also the designed software is considered to be reliable and is suitable to

perform real-time image reconstruction and mass flow rate measurements with an overall accuracy of about 85%.

References

[1] Abdul Rahim R, Chan KS, Pang JF, Leong L. A hardware development for optical tomography system using switch mode fan beam projection. Journal of Sensors & Actuators A: Physical 2005;120(1):277–90.

[2] Chan Kok San. Real time image reconstruction for fan beam optical tomography system. M.Sc. thesis. Universiti Teknologi Malaysia; 2002.

[3] Chan KS, Ruzairi AR. Tomographic imaging of pneumatic conveyor using optical sensor. In: 2nd world engineering congress. 2002.

[4] Green RG, Horbury NM, Abdul Rahim R, Dickin FJ, Naylor BD, Pridmore TP. Optical fibre sensors for process tomography. Measurement Science & Technology 1995;6:1699–704.

[5] Kak AC, Slaney Malcolm. Principles of Computerized Tomographic Imaging. Electronic ed. New York (United States): IEEE Press; 1999.

[6] Leong Lai Chen. Implementation of multiple fan beam projection technique in optical fibre process tomography. M.Sc. thesis. Universiti Teknologi Malaysia; 2005.

[7] Pang Jon Fea, Ruzairi Abdul Rahim, Chan Kok San. Infrared tomography sensor configuration using 4 parallel beam projections. In: 3rd international symposium on process tomography. 2004, p. 48–51.

[8] Ruzairi Abdul Rahim. A tomography imaging system for pneumatic conveyors using optical fibres. Ph.D. thesis. Sheffield Hallam University; 1996.

[9] Ibrahim Sallehuddin. Measurement of gas bubbles in a vertical water column using optical tomography. Ph.D. thesis. Sheffield Hallam University; 2000.

[10] Xu H, Dehghani H, Pogue PW, Springett R, Paulsen KD, Dunn JF. Near-infrared imaging in the small animal brain: Optimization of fiber positions. Journal of Biomedical Optics 2003;8(1):102–10.

R. Abdul Rahim received BEng. Degree with Honours in Electronic System And Control Engineering in 1992 from Sheffield City Polytechnic. He received his Ph.D. in Instrumentation & Electronics Engineering from Sheffield Hallam University in 1996. Currently he is a Deputy Dean (Corporate Services), Research Management Centre, Universiti Teknologi Malaysia. His current research interests are process tomography and process measurement.